

Simulation Study of a High-Order Mode BWO with Multiple Inclined Rectangular Electron Beams

Fengzhen Zhang^{1, 2, *}, Weilong Wang^{1, 2}, Zhaochuan Zhang¹, and Dongping Gao¹

Abstract—A backward wave oscillator (BWO) operating at the high-order mode (HOM) with multiple inclined rectangular electron beams (IRBs) is presented in this article. The BWO operating at the HOM with multiple IRBs (HOM IRB BWO) is driven by multiple IRBs. Compared with typical BWOs, the slow wave structure of the HOM IRB BWO is an overmoded metal-grating rectangular waveguide (OGRWG). The mode competition of the slow-wave device operating at the HOM is analyzed according to the ohmic losses of different modes of the OGRWG slow wave structure and multiple beams exciting. The analysis is verified by simulation. Two kinds of HOM-fundamental mode converters (MCs) are designed for converting the HOM generated by the HOM IRB BWO into the fundamental mode. The beam-wave interaction of the HOM IRB BWOs with the HOM-fundamental MC is studied. The results show that the mode competition does not occur; frequency spectrums of output signals are pure; and the HOM is converted into the fundamental mode effectively.

1. INTRODUCTION

Terahertz (THz) radiation sources driven by electron beams are widely used in high resolution radar imaging, wireless communication systems, spectral detection and biomedicine [1–4]. The THz radiation sources driven by electron beams include backward wave oscillators (BWOs) [5, 6], travelling wave tubes (TWTs) [7, 8], klystrons [9], gyrotrons [10], and extended interaction oscillators [11]. BWOs with sheet beam (SB BWOs) are slow wave devices (SWDs) and have the advantages of room-temperature operation, wide tuning bandwidths, small sizes, and low prices. SB BWO is one of the commonly used radiation sources in the sub-THz range. SB BWO is usually driven by one electron beam and operates at the fundamental mode. The size of the slow wave structure (SWS) of the SB BWO decreases with increasing operating frequencies because of the wavelength-size-matching effect. Therefore, the size of the electron beam involved in the beam-wave interaction is limited, and the size of the electron beam could not continue to increase when it increases to a certain extent. It is not easy to further increase the output power of the SB BWO when the current density of the electron beam is constant.

There are two ways to increase the output power without changing the current density of the electron beam. One way is to improve SB BWO into a clinotron. Clinotron was proposed by Levin et al. [12]. Some experimental studies and theoretical studies on clinotron have been studied [13–15]. The electron beam in clinotron is inclined to the SWS, which results in that more electrons involve in the beamwave interaction, and the output power is improved [16–18]. The other way is to make the SB BWO operate at the high-order mode (HOM). The geometrical size of the SWS of the SB BWO operating at the HOM would be larger, so the SB BWO operating at the HOM could accommodate the electron beam with a larger size when the operating frequencies are the same as the operating

Received 4 January 2021, Accepted 26 February 2021, Scheduled 7 March 2021

* Corresponding author: Fengzhen Zhang (zhangfengzhen16@mails.ucas.ac.cn).

¹ Key Laboratory of Science and Technology on High Power Microwave Sources and Technologies, Aerospace Information Research Institute, Chinese Academy of Sciences, Beijing 100190, China. ² School of Electronic, Electrical and Communication Engineering, University of Chinese Academy of Sciences, Beijing 100049, China.

frequencies of the SB BWO operating at the fundamental mode. Therefore, the output power could be improved. There are some researches on the SWD operating at the HOM (HOM SWD). Gong et al. have studied 140 GHz overmoded folded-waveguide TWT operating at the TE_{20} mode and driven by two cylindrical beams [19]. The simulation results showed that this TWT could work stably, and the frequency spectrum of the output signal was pure. Gee and Shin have studied 68–78 GHz dielectric-plate-implanted overmoded staggered double grating array TWT operating at the TM_{31} mode and driven by three elliptical beams [20]. Dielectric-plates implanted into the overmoded SWS suppress lower order modes and only allow the operating mode to propagate in the overmoded SWS. The simulation results showed that the mode competition of this TWT did not occur. Hu and Feng have studied W-band overmoded TWT operating at the TE_{20} mode and driven by two beams. PIC simulation results showed that the output power of this TWT was 800 W at 94 GHz [21]. Shi et al. have studied 220 GHz overmoded photonic crystal-loaded folded-waveguide TWT operating at the TE_{20} mode and driven by two sheet beams [22]. The simulation results showed that the mode competition of this TWT did not occur, and this TWT could generate output power of 128 W at 220 GHz. Shu et al. have studied 1.18–1.2 THz orthogonal grating waveguide BWO operating at TM_{51} -like mode and driven by five sheet beams [23, 24]. The simulation results showed that this BWO could work at TM_{51} -like π mode stably, and the frequency spectrum of the output signal was pure.

A BWO operating at the HOM with multiple inclined rectangular electron beams (IRBs) is presented in this article based on the existing research background [19–25]. The BWO operating at the HOM with multiple IRBs (HOM IRB BWO) is based on a BWO with an IRB (IRB BWO) in [25]. The SWS of the IRB BWO is extended to an overmoded structure. The HOM operation is implemented by multiple beams exciting. Mode converters (MCs) are designed to convert the HOM outputted from the HOM IRB BWO into the fundamental mode.

This article is organized as follows. An overmoded metal-grating rectangular waveguide (OGRWG) SWS is described, and the dispersion curves of the OGRWG SWS are calculated. The mode competition of the HOM SWD with the OGRWG SWS is analyzed and the analysis verified by simulation in Section 2. In Section 3, a TE_{20} - TE_{10} MC and a TE_{30} - TE_{10} MC are designed. The beam-wave interaction of the HOM IRB BWOs with a HOM-fundamental MC is studied in Section 4. In Section 5, the conclusions are given.

2. OGRWG SWS AND THE ANALYSIS OF THE MODE COMPETITION

2.1. Description of the OGRWG SWS

The SWS used in the HOM SWD in this article is the OGRWG and is shown in Fig. 1(a). The OGRWG SWS is similar to the typical metal-grating rectangular waveguide (GRWG) SWS which is shown in Fig. 1(b), and the only difference is the width of the waveguide. The width of the waveguide of the OGRWG SWS is the same as that of the grating of the OGRWG SWS. This width is denoted as a_w . The width of the waveguide of the GRWG SWS is also the same as that of the grating of the GRWG SWS. This width is denoted as a . The width of the waveguide of the OGRWG SWS is n times the width of the waveguide of the GRWG SWS, i.e., $a_w = na$. The dispersion curve of the TE_{xn0} mode (HOM) of the OGRWG SWS with a width of a_w is the same as that of the TE_{x10} mode (fundamental mode) of the GRWG SWS with a width of a , which would be verified later. The geometric models of the OGRWG SWS are shown in Fig. 1(c) and Fig. 1(d). The width of the groove, the depth of the groove, the height of the beam channel, and the length per period are denoted as d , h , D , and l , respectively.

Multiple electron beams are used in the HOM SWDs with the OGRWG SWS to excite the HOM electromagnetic fields and to make the electron beams interact with the electromagnetic fields effectively [19–24]. n electron beams are used if the HOM SWD operates at the TE_{xn0} mode. Fig. 1(d) shows the positional relationships between the emitting surfaces of the sheet beams and the beam channel of the HOM SWD operating at the TE_{x30} mode. The textured shadowing in Fig. 1(d) indicates the electron beams. There are three electron beams with the same geometric dimensions, and the center of each electron beam is located at the maximums of the electric fields. The width of each electron beam is w ; the thickness of the emitting surface of each electron beam is d_e ; the initial beam-grating distance is h_1 ; and the inclination angle of each electron beam is α . The direction of the focusing magnetic field B^{focus} is parallel to the propagation direction of the electron beam.

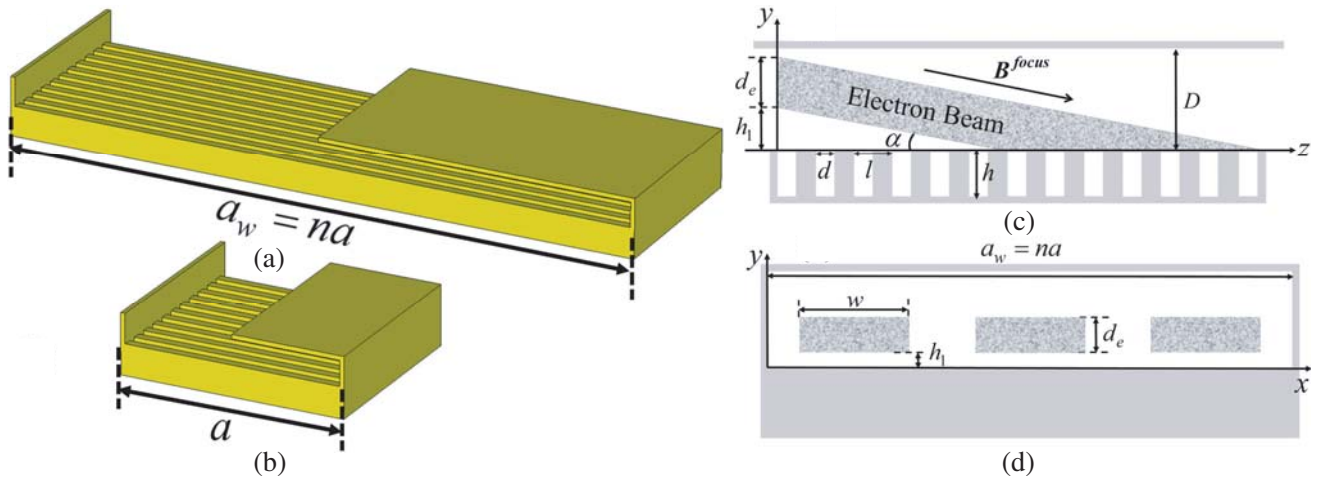


Figure 1. Models of the OGRWG SWS and the GRWG SWS. (a) Three-dimensional model of the OGRWG SWS. (b) Three-dimensional model of the GRWG SWS. (c) Axial cross-sectional view of the geometric model of the OGRWG SWS. (d) Transversal cross-sectional view of the geometric model of the OGRWG SWS and the positional relationship between the sheet beams and the beam channel.

The parameters of the GRWG SWS and the OGRWG SWS are $D = 0.2$ mm, $a = 1.71$ mm, $a_w = na$, $l = 0.14$ mm, $d = 0.07$ mm, and $h = 0.21$ mm [25]. The dispersion curves of the TE_{x10} mode of the GRWG SWS, the TE_{x20} mode of the OGRWG SWS ($n = 2$), and the first three modes of the OGRWG SWS ($n = 3$) are calculated and are shown in Fig. 2. For the dispersion curves of the first three modes of the OGRWG SWS ($n = 3$), the dispersion curve of the different modes move up with the increasing index number of the modes. The dispersion curves of the TE_{x10} mode of the GRWG SWS, the TE_{x20} mode of the OGRWG SWS ($n = 2$), and the TE_{x30} mode of the OGRWG SWS ($n = 3$) overlap, which means that the operating frequency band of the HOM SWD with the OGRWG SWS is the same as that of the SWD with the GRWG SWS. The HOM SWDs could be designed easily.

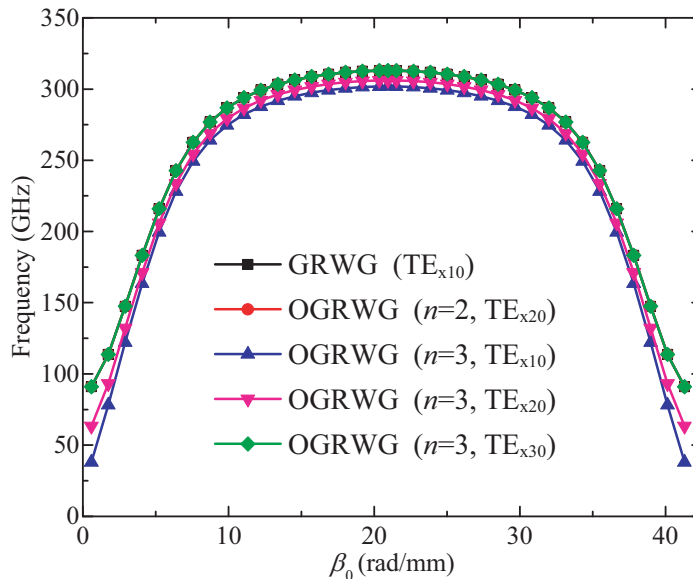


Figure 2. Dispersion curves of the TE_{x10} mode of the GRWG SWS, the TE_{x20} mode of the OGRWG SWS ($n = 2$), and the first three modes of the OGRWG SWS ($n = 3$).

2.2. Analysis of the Mode Competition

A case study of the HOM SWD operating at the TE_{x30} mode with the OGRWG SWS ($n = 3$) and three electron beams (TE_{x30} SWD) is performed to analyze the mode competition. The vector distributions of the electric fields of the first three modes of the single period of the OGRWG SWS ($n = 3$) with a phase shift of 105° are shown in Fig. 3. There is a phase difference with 180° between the left part and right part of the electric fields of the TE_{x20} mode in the x - y cross section. There is a phase difference with 180° between the left part and middle part of the electric fields of the TE_{x30} mode in the x - y cross section, and the phase of the left part is the same as the phase of the right part. The distributions of the electric fields of the TE_{x20} mode in the x - y cross section are antisymmetric, and it is difficult to excite the antisymmetric mode by three symmetrically distributed electron beams [17, 26]. Therefore, the TE_{x20} mode could not be excited. The ohmic losses of the first three modes of the OGRWG SWS ($n = 3$) are shown in Fig. 4(a). At the same frequency, the ohmic losses of the TE_{x10} mode and TE_{x20} mode are larger than the ohmic losses of the TE_{x30} mode, which means that the lower order modes could be attenuated effectively, and the stable oscillation of the TE_{x10} mode is not easily established. Therefore, the mode competition of the TE_{x30} SWD is not prone to occur.

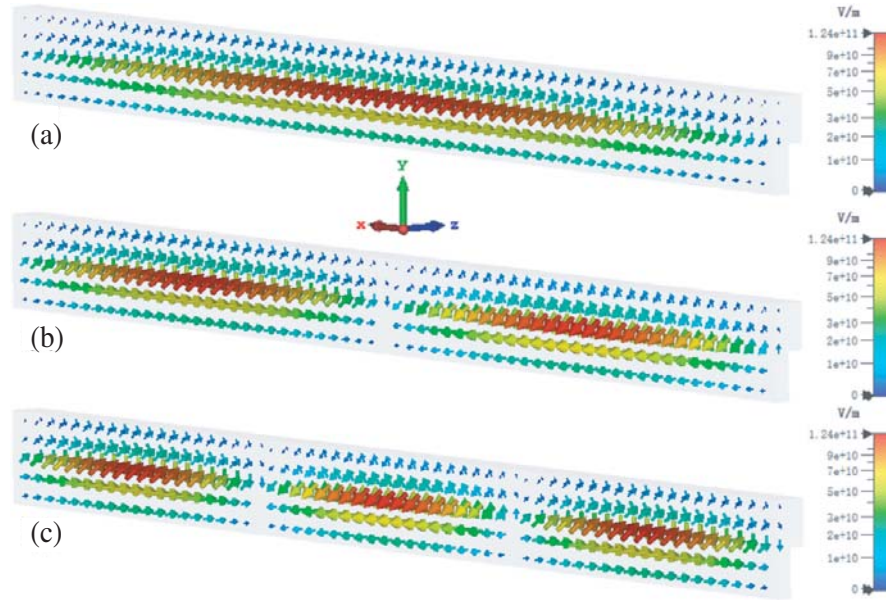


Figure 3. Vector distributions of the electric fields of the first three modes of the single period of the OGRWG SWS ($n = 3$) with a phase shift of 105° . (a) TE_{x10} mode. (b) TE_{x20} mode. (c) TE_{x30} mode.

For the HOMSWD operating at the TE_{x20} mode with the OGRWG SWS ($n = 2$) and two electron beams (TE_{x20} SWD), the antisymmetric TE_{x20} mode could be excited by two symmetrically distributed electron beams. The ohmic losses of the TE_{x10} mode and TE_{x20} mode of the OGRWG SWS ($n = 2$) are shown in Fig. 4(b). At the same frequency, the ohmic losses of the TE_{x10} mode are larger than those of the TE_{x20} mode. The maximum electric field of the TE_{x10} mode is located at the center of the waveguide, and it is difficult for two symmetrically distributed electron beams to interact with the TE_{x10} mode effectively [19]. Therefore, the mode competition of the TE_{x20} SWD is not prone to occur.

2.3. Verification of the Analysis

The analysis of the mode competition is verified by the simulation software. The HOM SWDs used for the verification are HOM IRB BWOs. The model of the HOM IRB BWO operating at the TE_{x20} mode with the OGRWG SWS ($n = 2$) and two electron beams (TE_{x20} IRB BWO) is shown in Fig. 5(a) [25]. The light blue part indicates the vacuum, and the background material is the oxygen-free copper with a conductivity of 2.2×10^7 S/m. The output coupler (six combs with gradual varying groove depths)

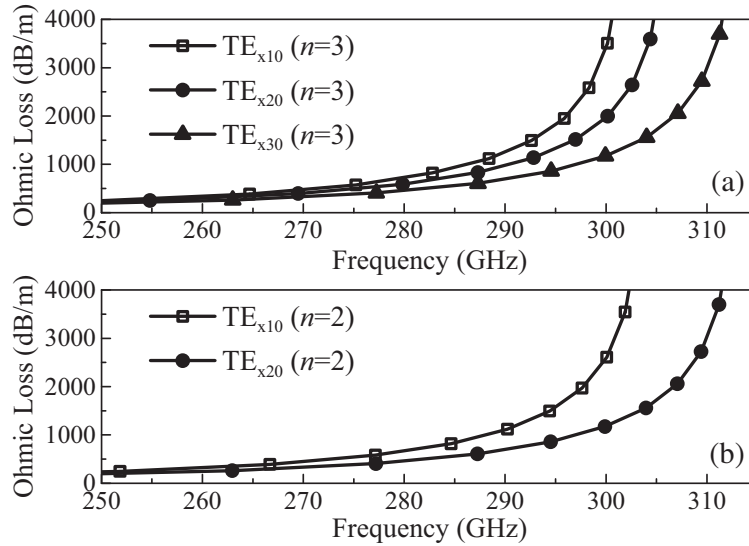


Figure 4. Ohmic losses of different modes of the OGRWG SWS. (a) OGRWG SWS ($n = 3$). (b) OGRWG SWS ($n = 2$).

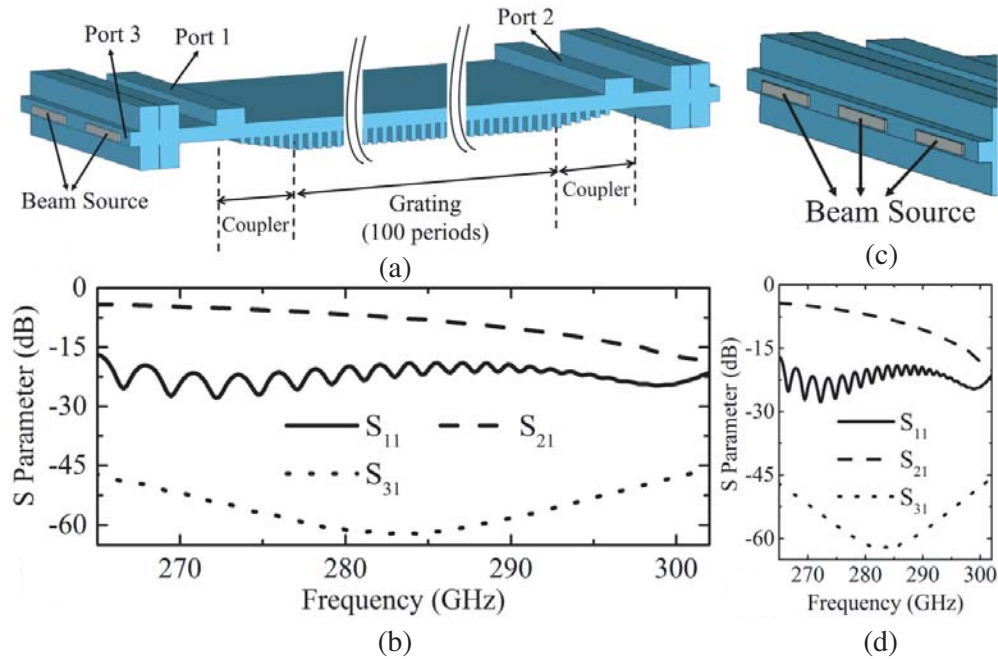


Figure 5. Models of the HOM IRB BWOs and their transmission characteristics. (a) Model of the TE_{x20} IRB BWO. (b) S -parameters of the TE_{x20} IRB BWO. (c) Electron beams of the TE_{x30} IRB BWO. (d) S -parameters of the TE_{x30} IRB BWO.

transmits the TE_{xn0} mode in the SWS to the TE_{n0} mode. Fig. 5(b) is the transmission characteristics of the TE_{x20} IRB BWO. The model of the HOM IRB BWO operating at the TE_{x30} mode with the OGRWG SWS ($n = 3$) and three electron beams (TE_{x30} IRB BWO) is similar to the model of the TE_{x20} IRB BWO. The only difference between these models is the electron beams, and the distribution of the electron beams of the TE_{x30} IRB BWO is shown in Fig. 5(c). Fig. 5(d) is the transmission characteristics of the TE_{x30} IRB BWO. S_{11} (the reflection coefficients) of these models is less than -19 dB, and S_{31} is less than -45 dB, which means that the transmission characteristics of the interaction systems are

good.

The beam-wave interaction is simulated based on the above models. The geometric parameters, the current density and the beam voltage of each electron beam are the same. The width of each electron beam is $w = 1.026$ mm; the thickness of the emitting surface of each electron beam is $d_e = 0.112$ mm; the initial beam-grating distance is $h_1 = 0.01$ mm; the inclination angle of each electron beam is $\alpha = 0.35^\circ$; the current density of each electron beam is $J = 40$ A/cm², i.e., the current of each electron beam is $I_0 = 46$ mA. The focusing magnetic field is $B = 0.6$ T, and the direction of \mathbf{B} is parallel to the propagation direction of the electron beams.

When the beam voltage is 9.13 kV, Fig. 6(a) shows the signal power of different modes observed at the output port (port 1) of the TE_{x20} IRB BWO versus time, and Fig. 6(b) shows the frequency spectrum of the output signal of the TE₂₀ mode. The signal power of the TE₂₀ mode increases rapidly to 5.1 W and then decreases slightly. The signal power of the TE₂₀ mode is stable at 4.94 W after 5.5 ns, and the electronic efficiency is 0.59%. The illustration in Fig. 6(a) shows the amplification of the signal power of the TE₁₀ mode. The signal power of the TE₁₀ mode is much less than that of the TE₂₀ mode, which means that the TE₁₀ mode is not excited. The frequency spectrum of the signal of the TE₂₀ mode is pure, and the operating frequency is 292.75 GHz. Therefore, mode competition does not occur during the operation of the TE_{x20} IRB BWO.

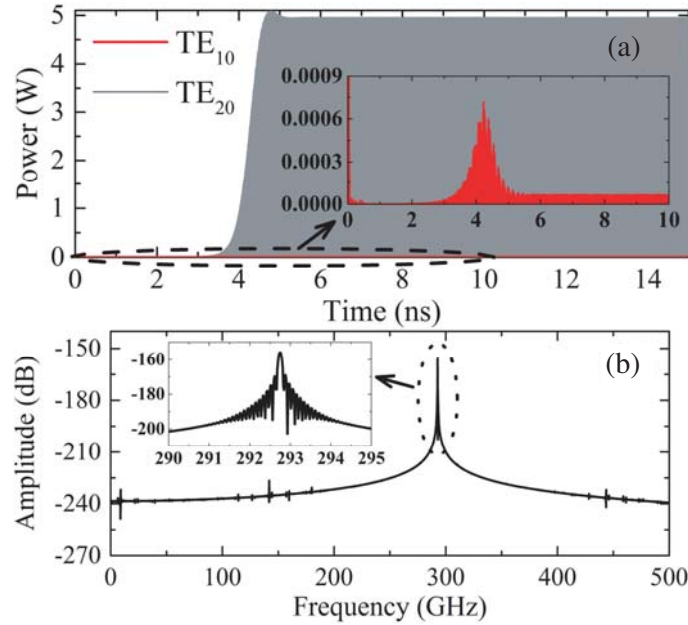


Figure 6. PIC simulation results of the TE_{x20} IRB BWO. (a) Signal power observed at the output port versus time. (b) Frequency spectrum of the output signal of the TE₂₀ mode.

The PIC simulation results of the TE_{x30} IRB BWO at the beam voltage of 9.13 kV are shown in Fig. 7. The signal power of the TE₃₀ mode is stable at 6.84 W after 6 ns, and the electronic efficiency is 0.54%. The amplification of the signal power of the TE₁₀ mode and TE₂₀ mode is shown in the illustration in Fig. 7(a). The signal powers of the TE₁₀ mode and TE₂₀ mode are much less than that of the TE₃₀ mode, which means that the device only outputs the TE₃₀ mode, and the mode competition does not occur. The frequency spectrum of the output signal of the TE₃₀ mode is pure, and the operating frequency is 292.78 GHz. This operating frequency is approximately equal to the operating frequency of the TE_{x20} IRB BWO, which is consistent with the analysis of the dispersion curves. The PIC simulation results above verify the analysis of the mode competition.

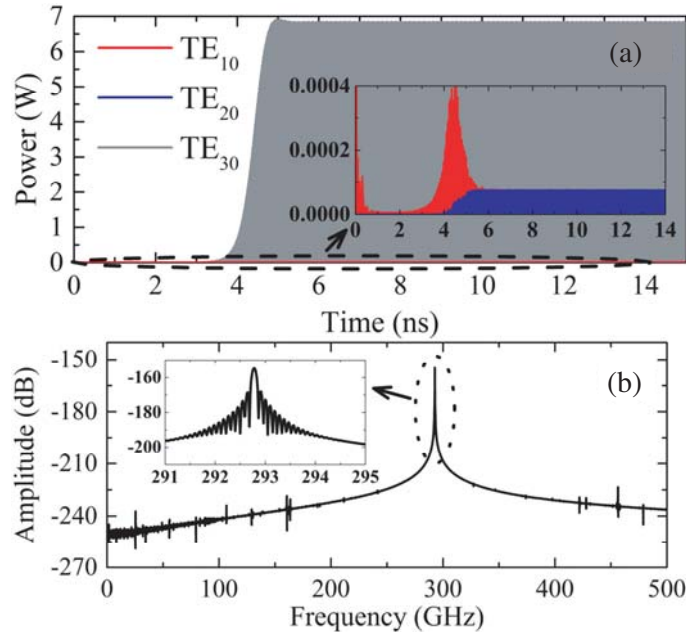


Figure 7. PIC simulation results of the TE_{x30} IRB BWO. (a) Signal power observed at the output port versus time. (b) Frequency spectrum of the output signal of the TE_{30} mode.

3. MODE CONVERTER

3.1. TE_{n0} - TE_{10} MC

The output signal of the HOM IRB BWOs designed in the previous section is the HOM electromagnetic waves. However, not all applications require the HOM electromagnetic waves. Many applications require the fundamental mode electromagnetic waves, such as the multi-way microwave power combiner and high-power microwave feed antennas [27, 28]. The HOM SWDs with the MC could be used in more applications. Therefore, it is necessary to design the MCs to convert the TE_{n0} mode (HOM) output from the output port into the TE_{10} mode (fundamental mode). For the TE_{x20} IRBBWO and TE_{x30} IRBBWO designed in the previous section, the TE_{20} - TE_{10} MC and TE_{30} - TE_{10} MC are designed.

There are several ways to realize converting the rectangular waveguide HOM into the fundamental mode. (1) A rectangular waveguide MC with a nonsymmetrical H -plane corner could convert the TE_{n0} mode into the TE_{10} mode [29]. (2) A TE_{n0} - TE_{10} MC with the rectangular coupling apertures is formed by an overmoded rectangular input waveguide connected to an orthogonal rectangular output waveguide by $(n - 1)$ rectangular coupling apertures [30]. In order to reduce the reflection and suppress the unwanted modes, rectangular septa are inserted in the output waveguide, and $(n - 1)$ rectangular recesses are added at the bottom of the overmoded input waveguide [31]. (3) An H -plane T-junction is used to realize the conversion from the TE_{20} mode to the TE_{10} mode. This MC consists of an overmoded input waveguide, two vice branch waveguides, a septum, two irises, and an output waveguide. This MC could achieve high conversion efficiency and low reflection in a wide frequency range [32]. (4) A dual-bend TE_{20} - TE_{10} MC and a tri-bend TE_{20} - TE_{10} MC are formed by serpentine metal pipes and could easily realize the mode conversion [33].

The TE_{20} - TE_{10} MC for the TE_{x20} IRB BWO is designed based on the H -plane T-junction MC. The TE_{30} - TE_{10} MC for the TE_{x30} IRB BWO is designed based on the TE_{n0} - TE_{10} MC with the rectangular coupling apertures.

The width of the longest side of the output waveguide of the TE_{x20} IRB BWO is equal to a_w . The width of the longest side of the overmoded input waveguide of the TE_{20} - TE_{10} MC is denoted as a_{mc} . a_w is too broad, and it is difficult to design a structure that could realize the mode conversion if $a_{mc} = a_w$. Therefore, a_{mc} needs to be shortened. The Chebyshev multisection matching transformer is

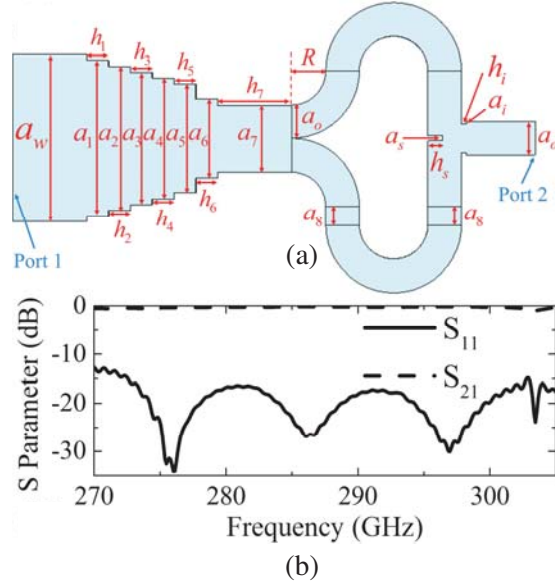


Figure 8. Model of the TE₂₀-TE₁₀ MC and its transmission characteristics. (a) Model. (b) S -parameters.

a common microwave element for transferring waveguides of different sizes [34]. The transferring from the output waveguide of the TE _{x 20} IRB BWO to the input waveguide of the TE₂₀-TE₁₀ MC could be realized by Chebyshev multisection matching transformers. Therefore, the overmoded input waveguide of the TE₂₀-TE₁₀ MC based on the model in [32] is connected with a Chebyshev multisection matching transformer, and the model of the TE₂₀-TE₁₀ MC is shown in Fig. 8(a). The thickness of the MC is the same as the width of the shortest side of the output waveguide of the TE _{x 20} IRB BWO, and the thickness is 0.417 mm. The other geometric parameters of the MC are listed in Table 1. The background material of the model is the oxygen-free copper with a conductivity of 2.2×10^7 S/m. The transmission characteristics of the TE₂₀-TE₁₀ MC are shown in Fig. 8(b). $S_{11} < -15$ dB and $S_{21} > -0.4$ dB in the range of 273–302 GHz show that the MC has good transmission characteristics. The losses of the power during the transmission are less than 5%.

Table 1. Geometric parameters of the TE₂₀-TE₁₀ MC.

Parameter	a_o	a_i	a_s	a_w	a_1	a_2
Value	0.682	0.05	0.1	3.42	3.18	2.94
Parameter	a_3	a_4	a_5	a_6	a_7	a_8
Value	2.7	2.46	2.22	1.604	1.364	0.4
Parameter	h_i	h_s	h_1	h_2	h_3	h_4
Value	0.1	0.3	0.445	0.445	0.445	0.445
Parameter	h_5	h_6	h_7	R		
Value	0.445	0.445	1.5	0.7		

*unit mm

The model of the TE₃₀-TE₁₀ MC is shown in Fig. 9(a), and the geometric parameters of the MC are listed in Table 2. Similar to the TE₂₀-TE₁₀ MC, the overmoded input waveguide of the TE₃₀-TE₁₀ MC based on the model in Reference [31] is connected with a Chebyshev multisection matching transformer. The width of the shortest side of the Chebyshev transformer is the same as the width of the shortest

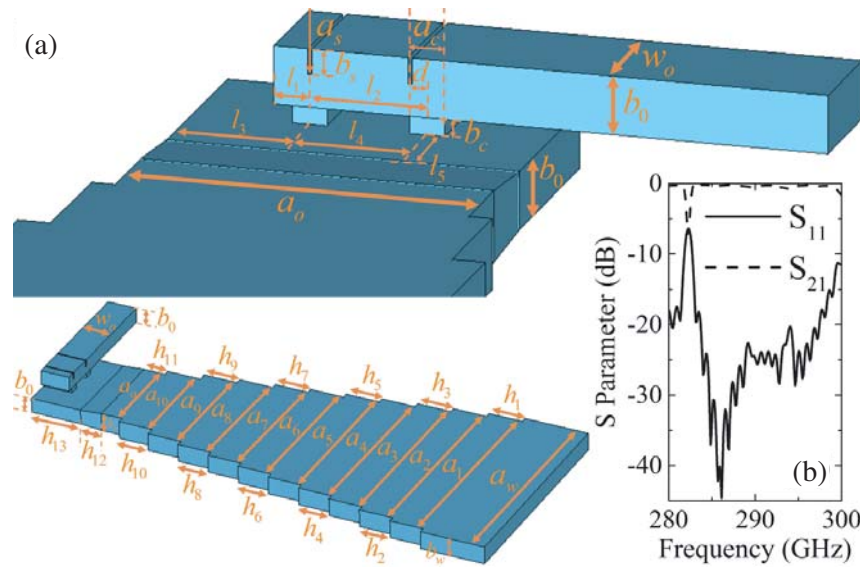


Figure 9. Model of the TE₃₀-TE₁₀ MC and its transmission characteristics. (a) Model. (b) *S*-parameters.

side of the output waveguide of the TE_{x30} IRB BWO, and this width is denoted as b_w . The width of the shortest side of the overmoded input waveguide of the TE₃₀-TE₁₀ MC is denoted as b_0 . Different from the TE₂₀-TE₁₀ MC, b_0 is slightly smaller than b_w . Therefore, the two parts are connected by a tapered transferring structure with a length of h_{12} . The transmission characteristics of the TE₃₀-TE₁₀ MC are shown in Fig. 9(b). $S_{11} < -15$ dB and $S_{21} > -1$ dB in the range of 283–299 GHz show that the transmission characteristics are good. The losses of the power during the transmission are less than 10%.

Table 2. Geometric parameters of the TE₃₀-TE₁₀ MC.

Parameter	w_o	b_o	a_s	a_c	b_s	b_c
Value	0.682	0.341	0.026	0.2	0.15	0.1
Parameter	d	l_1	l_2	l_3	l_4	l_5
Value	0.1	0.21	0.682	0.682	0.682	0.5
Parameter	a_o	a_w	a_1	a_2	a_3	a_4
Value	2.046	5.13	4.86	4.59	4.32	4.05
Parameter	a_5	a_6	a_7	a_8	a_9	a_{10}
Value	3.78	3.51	3.24	2.97	2.7	2.316
Parameter	b_w	h_1	h_2	h_3	h_4	h_5
Value	0.417	0.784	0.784	0.784	0.784	0.784
Parameter	h_6	h_7	h_8	h_9	h_{10}	h_{11}
Value	0.784	0.784	0.784	0.784	0.784	0.5
Parameter	h_{12}	h_{13}				
Value	0.5	1.182				

*unit mm

3.2. Model of the HOM IRB BWO with the MC

The HOM IRB BWO outputting TE_{10} mode is obtained by connecting the HOM IRB BWO with the MC. Fig. 10(a) is the model of the TE_{x20} IRB BWO with the TE_{20} - TE_{10} MC (TE_{x20} MC IRB BWO). The number of meshes would be very large, and the PIC simulation could be continued if the MC is connected to the HOM IRB BWO vertically. The number of meshes required for the PIC simulation could be significantly reduced by connecting the MC to the HOM IRB BWO by a 90° bend waveguide. Fig. 10(c) is the transmission characteristics of this model. $S_{11} < -15$ dB in the range of 285–305 GHz shows that the interaction system has good transmission characteristics. Fig. 10(b) is the model of the TE_{x30} IRB BWO with the TE_{30} - TE_{10} MC (TE_{x30} MC IRB BWO), and Fig. 10(d) is the transmission characteristics of this model. $S_{11} < -15$ dB in the range of 286–301 GHz shows that the interaction system could meet the requirements of the application.

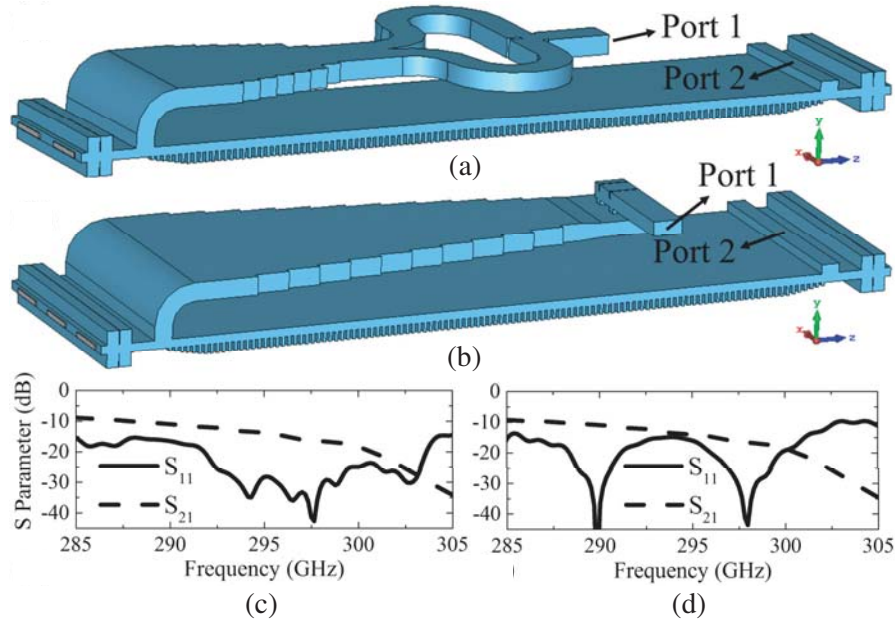


Figure 10. Models of the HOM IRB BWOs with the MC and these transmission characteristics. (a) Model of the TE_{x20} MC IRB BWO. (b) Model of the TE_{x30} MC IRB BWO. (c) S -parameters of the TE_{x20} MC IRB BWO. (d) S -parameters of the TE_{x30} MC IRB BWO.

4. THE BEAM-WAVE INTERACTION OF THE HOM IRB BWO WITH THE MC

The HOMIRB BWOs with the MC are simulated. The parameters of the electron beams are the same as those in Section 2. When the beam voltage is 9.13 kV, the arrows plots and contour plots of the electric field distributions in the x - z cross section of the MC of the TE_{x20} MC IRB BWO are shown in Fig. 11. The TE_{20} mode generated by the TE_{x20} IRB BWO passes through the MC and converts into the TE_{10} mode. The signal power of different modes observed at the output port (port 1) of the TE_{x20} MC IRB BWO versus time and the frequency spectrum of the output signal of the TE_{10} mode are shown in Fig. 12. The signal powers of the TE_{20} mode and TE_{30} mode are much less than that of the TE_{10} mode, which means that the mode of the signal of the output port is the TE_{10} mode. The signal power is stable at 4.73 W after 6 ns, and the electronic efficiency is 0.56%. The frequency spectrum of the output signal of the TE_{10} mode is pure, and the operating frequency is 292.64 GHz. Compared with the TE_{x20} IRB BWO without the MC, the output power of the TE_{x20} MC IRB BWO is reduced by 4.25%, which is consistent with the losses of less than 5% for the TE_{20} - TE_{10} MC. The power losses after connecting with the MC are mainly caused by the ohmic losses of the MC.

For the TE_{x30} MC IRB BWO when the beam voltage is 9.13 kV, the arrows plots of the electric field

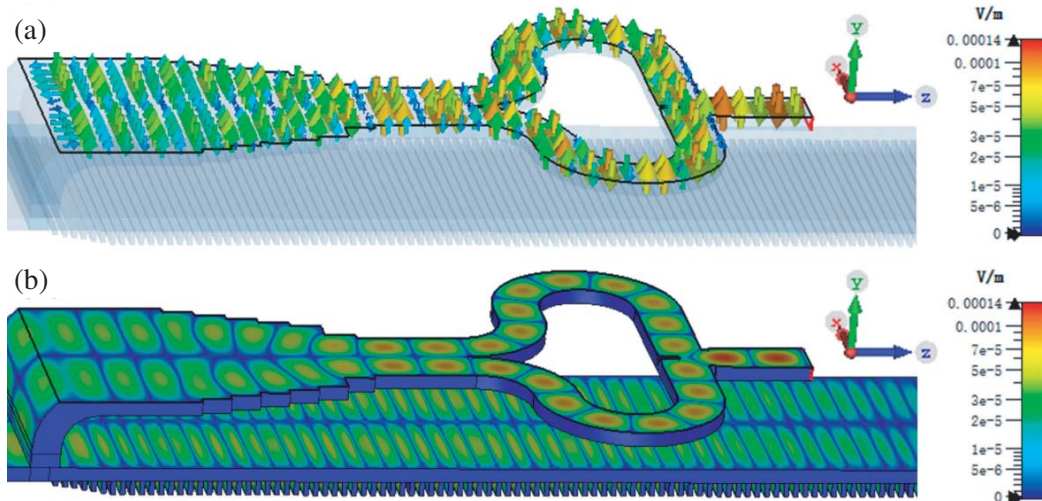


Figure 11. Electric field distributions in the x - z cross section of the MC of the TE_{x20} MC IRB BWO. (a) Arrows plots. (b) Contour plots.

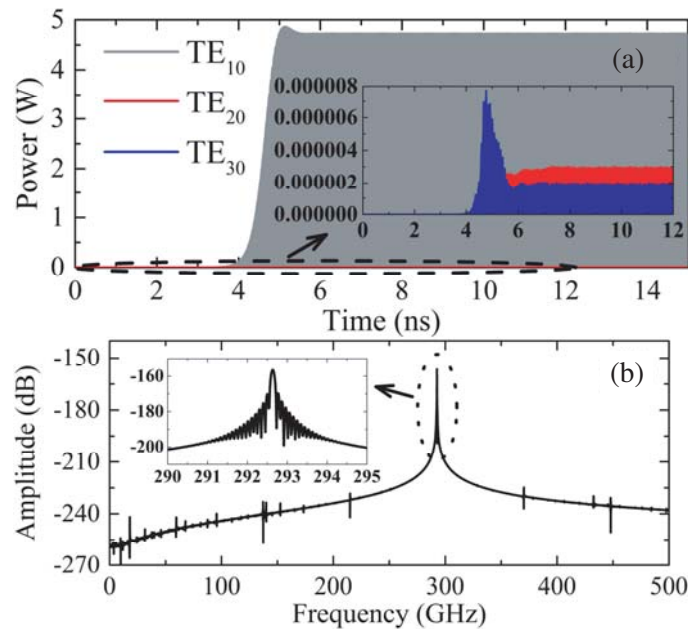


Figure 12. PIC simulation results of the TE_{x20} MC IRB BWO. (a) Signal power observed at the output port versus time. The illustration shows the amplification of the signal power of the TE_{20} mode and the TE_{30} mode. (b) Frequency spectrum of the output signal of the TE_{10} mode.

distributions in the x - z cross section of the MC and the contour plots of the electric field distributions of the model are shown in Fig. 13. The TE_{30} mode generated by the TE_{x30} IRB BWO passes through the MC and converts into the TE_{10} mode. Fig. 14 shows the PIC simulation results of the TE_{x30} MC IRB BWO. The signal powers of the TE_{20} mode, TE_{30} mode, and TE_{40} mode are much less than that of the TE_{10} mode, which means that the device only outputs the TE_{10} mode. The signal power is stable at 5.91 W after 6.2 ns, and the electronic efficiency is 0.47%. The frequency spectrum of the output signal of the TE_{10} mode is pure, and the operating frequency is 292.95 GHz. Compared with the TE_{x30} IRB BWO without the MC, the output power of the TE_{x30} MC IRB BWO is reduced by 13.6%. However, the power losses should be less than 10%. The field distributions in the SWS change to some extent

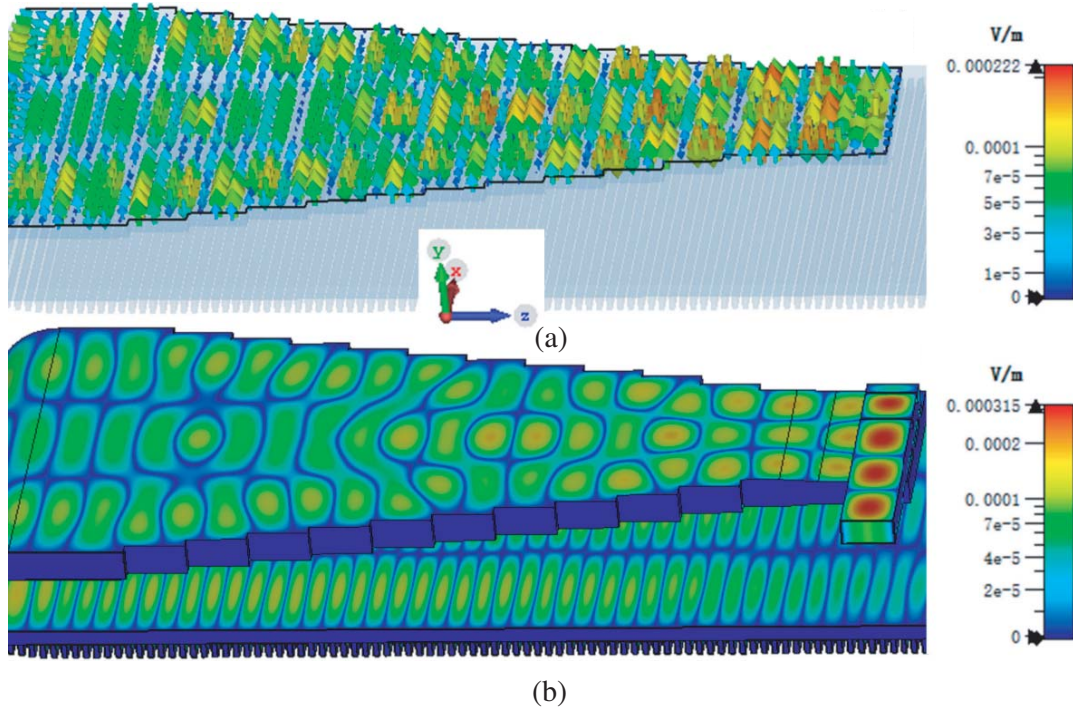


Figure 13. Electric field distributions of the TE_{x30} MC IRB BWO. (a) Arrows plots of the electric field distributions in the x - z cross section of the MC. (b) Contour plots of the electric field distributions of the model.

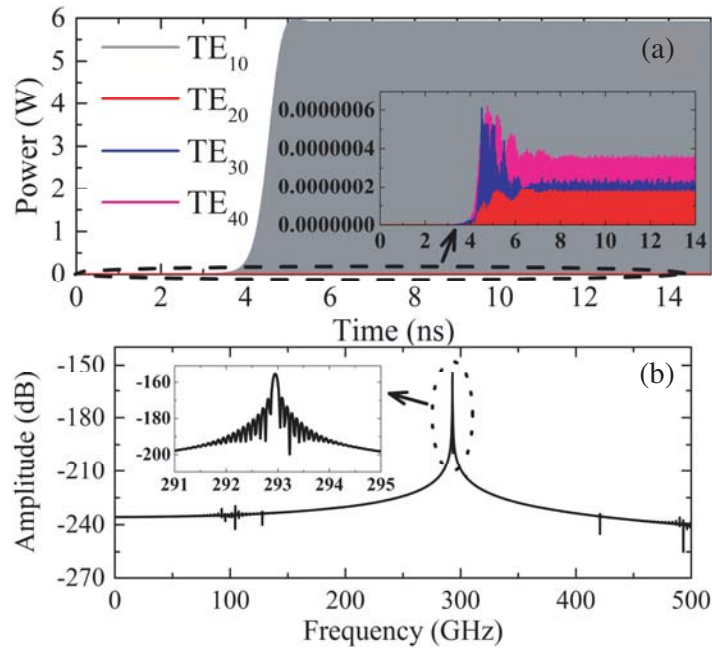


Figure 14. PIC simulation results of the TE_{x30} MC IRB BWO. (a) Signal power observed at the output port versus time. The illustration shows the amplification of the signal power of TE_{20} mode the TE_{30} mode and the TE_{40} mode. (b) Frequency spectrum of the output signal of the TE_{10} mode.

because of the addition of the 90° bend waveguide, the Chebyshev multisection matching transformer, and the MC, which affects the beam-wave interaction. As a result, the output power drops more.

Figure 15(a) shows the output characteristic and the operating frequencies versus beam voltages of the TE_{x20} MC IRB BWO in the range of 8.2–11.4 kV. The output power decreases from 4.74 W to 2.76 W, and the operating frequency increases from 286.78 GHz to 302.27 GHz with increasing beam voltage. The output characteristic and the operating frequencies versus beam voltages of the TE_{x30} MC IRB BWO are shown in Fig. 15(b) when the beam voltage is varied from 8.2 kV to 10.6 kV. The output power decreases from 6 W to 4.39 W, and the operating frequency increases from 287.05 GHz to 299.76 GHz with an increase in beam voltage.

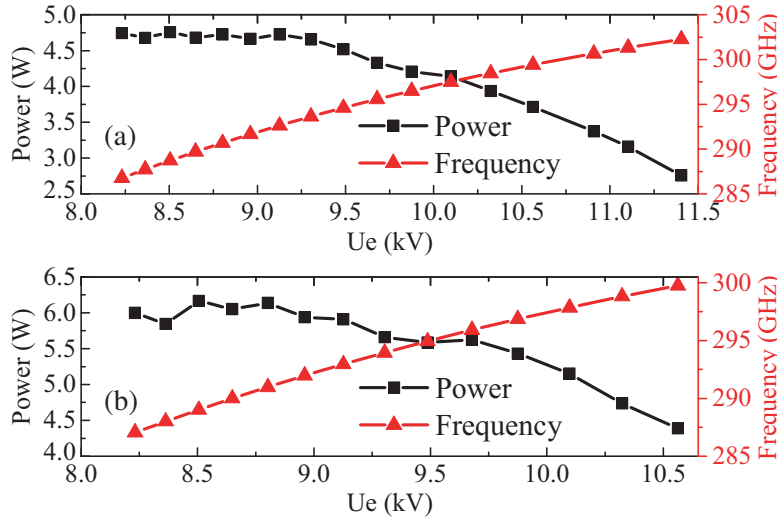


Figure 15. Output characteristics and operating frequencies versus beam voltages of the HOM IRB BWOs with the MC. (a) TE_{x20} MC IRB BWO. (b) TE_{x30} MC IRB BWO.

5. CONCLUSION

The OGRWG SWS used in the HOM IRB BWO is described. The dispersion curves and the ohmic losses of different modes of the OGRWG SWS are calculated. It is analyzed that the mode competition does not occur when the HOM SWDs with the OGRWG SWS operate at the HOM according to the ohmic losses of different modes of the OGRWG SWS and the multiple beams exciting. The PIC simulation results show that the TE_{x20} IRB BWO with two electron beams and TE_{x30} IRB BWO with three electron beams could operate at the HOM stably, and the mode competition does not occur. The TE_{x20} IRB BWO outputs the TE₂₀ mode with the power of 4.94 W; the electronic efficiency is 0.59%, and the operating frequency is 292.75 GHz when the beam voltage is 9.13 kV. The TE_{x30} IRB BWO outputs the TE₃₀ mode with the power of 6.84 W; the electronic efficiency is 0.54%, and the operating frequency is 292.78 GHz when the beam voltage is 9.13 kV. The TE₂₀-TE₁₀ MC and TE₃₀-TE₁₀ MC are designed and connected with the HOM IRB BWOs. The beam-wave interaction of the HOM IRB BWOs with the MC is studied. The PIC simulation results show that the MCs convert the HOM generated by the HOM IRB BWOs into the fundamental mode effectively. The TE_{x20} MC IRB BWO outputs the TE₁₀ mode with the power of 4.73 W; the electronic efficiency is 0.56%, and the operating frequency is 292.64 GHz when the beam voltage is 9.13 kV. The TE_{x30} MC IRB BWO outputs the TE₁₀ mode with the power of 5.91 W; the electronic efficiency is 0.47%, and the operating frequency is 292.95 GHz when the beam voltage is 9.13 kV. Compared with the HOM IRB BWO without the MC, the output power of the HOM IRB BWO with the MC is reduced, which is mainly caused by the losses of the MCs and the influence of the MCs on the electromagnetic fields of the SWS. These results offer reference values for designing the HOM BWO and exploring the beam-wave interaction of the HOM BWO.

REFERENCES

1. Alexander, N. E., B. Alderman, F. Allona, et al., "TeraSCREEN: Multi-frequency multi-mode Terahertz screening for border checks," *Passive and Active Millimeter-Wave Imaging XVII*, Vol. 9078, 907802, International Society for Optics and Photonics, 2014.
2. Hirata, A., T. Kosugi, H. Takahashi, et al., "120-GHz-band millimeter-wave photonic wireless link for 10-Gb/s data transmission," *IEEE Transactions on Microwave Theory and Techniques*, Vol. 54, No. 5, 1937–1944, 2006.
3. Joyce, H. J., C. J. Docherty, Q. Gao, et al., "Electronic properties of GaAs, InAs and InP nanowires studied by terahertz spectroscopy," *Nanotechnology*, Vol. 24, No. 21, 214006, 2013.
4. Yang, X., X. Zhao, K. Yang, et al., "Biomedical applications of terahertz spectroscopy and imaging," *Trends in Biotechnology*, Vol. 34, No. 10, 810–824, 2016.
5. Xie, W., Z. C. Wang, J. Luo, et al., "Three dimensional nonlinear analysis of a single-grating rectangular waveguide Cerenkov maser," *Physics of Plasmas*, Vol. 22, No. 4, 042307, 2015.
6. Mineo, M. and C. Paoloni, "Comparison of THz backward wave oscillators based on corrugated waveguides," *Progress In Electromagnetics Research*, Vol. 30, 163–171, 2012.
7. He, T., Z. L. Wang, X. Li, et al., "Study on silicon-based conformal microstrip angular log-periodic meander line traveling wave tube," *Progress In Electromagnetics Research*, Vol. 75, 29–37, 2018.
8. Lu, F., M. Grieser, C. Zhang, et al., "3-D nonlinear theory for sheet-beam folded-waveguide traveling-wave tubes," *IEEE Transactions on Electron Devices*, Vol. 65, No. 11, 5103–5110, 2018.
9. Zhang, Z., J. Luo, Z. Zhang, et al., "S-band Klystron with 300 MHz bandwidth at 850 kW peak power and 20 kW average power," *Progress In Electromagnetics Research*, Vol. 103, 177–186, 2020.
10. Glyavin, M. Y., A. G. Luchinin, G. S. Nusinovich, et al., "A 670 GHz gyrotron with record power and efficiency," *Applied Physics Letters*, Vol. 101, No. 15, 153503, 2012.
11. Zhang, X., R. Zhang, and Y. Wang, "Research on a high-order mode multibeam extended-interaction oscillator with coaxial structure," *IEEE Transactions on Plasma Science*, Vol. 48, No. 6, 1902–1909, 2020.
12. Levin, C. Y., A. Y. Kirichenko, A. I. Borodkin, et al., "The clinotron," *1992 22nd European Microwave Conference*, Vol. 1, 603–607, IEEE, 1992.
13. Schunemann, K. and D. M. Vavriv, "Theory of the clinotron: A grating backward-wave oscillator with inclined electron beam," *IEEE Transactions on Electron Devices*, Vol. 46, No. 11, 2245–2252, 1999.
14. Vavriv, D. M., "Potential of the Clinotron for THz-generation," *AIP Conference Proceedings*, Vol. 807, No. 1, 367–372, American Institute of Physics, 2006.
15. Andrushkevich, V. S., Y. G. Gamayunov, and E. V. Patrusheva, "A nonlinear clinotron theory," *Journal of Communications Technology and Electronics*, Vol. 55, No. 3, 330–336, 2010.
16. Sattorov, M., E. Khutoryan, K. Lukin, et al., "Improved efficiency of backward-wave oscillator with an inclined electron beam," *IEEE Transactions on Electron Devices*, Vol. 60, No. 1, 458–463, 2012.
17. Xi, H., Z. He, J. Wang, et al., "A continuous-wave clinotron at 0.26 THz with sheet electron beam," *Physics of Plasmas*, Vol. 24, No. 3, 033105, 2017.
18. Ponomarenko, S. S., S. A. Kishko, V. V. Zavertanniy, et al., "400-GHz continuous-wave clinotron oscillator," *IEEE Transactions on Plasma Science*, Vol. 41, No. 1, 82–86, 2012.
19. Gong, Y., H. Yin, L. Yue, et al., "A 140-GHz two-beam overmoded folded-waveguide traveling-wave tube," *IEEE Transactions on Plasma Science*, Vol. 39, No. 3, 847–851, 2011.
20. Gee, A. and Y. M. Shin, "Gain analysis of higher-order-mode amplification in a dielectric-implanted multi-beam traveling wave structure," *Physics of Plasmas*, Vol. 20, No. 7, 073106, 2013.
21. Hu, Y. and J. Feng, "Research of kilowatts W-band overmoded TWT," *2015 8th UK, Europe, China Millimeter Waves and THz Technology Workshop (UCMMT)*, 1–3, IEEE, 2015.
22. Shi, N., H. Wang, D. Xu, et al., "Study of 220 GHz dual-beam overmoded photonic crystal-loaded folded waveguide TWT," *IEEE Transactions on Plasma Science*, Vol. 47, No. 6, 2971–2978, 2019.

23. Shu, G. X., G. Liu, and Z. F. Qian, "Simulation study of a high-order mode terahertz radiation source based on an orthogonal grating waveguide and multiple sheet electron beams," *Optics Express*, Vol. 26, No. 7, 8040–8048, 2018.
24. Shu, G., G. Liu, L. Chen, et al., "Terahertz backward wave radiation from the interaction of high-order mode and double sheet electron beams," *Journal of Physics D: Applied Physics*, Vol. 51, No. 5, 055107, 2018.
25. Zhang, F., Z. Zhang, D. Gao, et al., "A 3-D frequency-domain nonlinear theory of the BWO with an inclined rectangular electron beam," *IEEE Transactions on Plasma Science*, Vol. 48, No. 9, 3040–3046, 2020.
26. Xi, H., J. Wang, Z. He, et al., "Continuous-wave Y-band planar BWO with wide tunable bandwidth," *Scientific Reports*, Vol. 8, No. 1, 1–7, 2018.
27. Chang, C., Z. Xiong, L. Guo, et al., "Compact four-way microwave power combiner for high power applications," *Journal of Applied Physics*, Vol. 115, No. 21, 214502, 2014.
28. Chang, C., X. Zhu, G. Liu, J. Fang, R. Xiao, C. Chen, H. Shao, J. Li, H. Huang, Q. Zhang, and Z.-Q. Zhang, "Design and experiments of the GW high-power microwave feed horn," *Progress In Electromagnetics Research*, Vol. 101, 157–171, 2010.
29. Kirilenko, A. A., L. A. Rud, and V. I. Tkachenko, "Nonsymmetrical H -plane corners for TE_{10} - TE_{q0} mode conversion in rectangular waveguides," *IEEE Transactions on Microwave Theory and Techniques*, Vol. 54, No. 6, 2471–2477, 2006.
30. Liu, G., Y. Wang, Y. Pu, et al., "Design and microwave measurement of a novel compact TE_{0n} - $TE_{1n'}$ mode converter," *IEEE Transactions on Microwave Theory and Techniques*, Vol. 64, No. 12, 4108–4116, 2016.
31. Shu, G., Z. Cai, Y. Li, et al., "Wideband rectangular TE_{10} to TE_{0n} mode converters for terahertz-band high-order overmoded planar slow-wave structures," *IEEE Transactions on Electron Devices*, Vol. 67, No. 3, 1259–1265, 2020.
32. Shu, G., Z. Qian, and W. He, "Design and measurement of an H-band rectangular TE_{10} to TE_{20} mode converter," *IEEE Access*, Vol. 8, 37242–37249, 2020.
33. Zhang, Q., C. W. Yuan, and L. Liu, "Theoretical design and analysis for TE_{20} - TE_{10} rectangular waveguide mode converters," *IEEE Transactions on Microwave Theory and Techniques*, Vol. 60, No. 4, 1018–1026, 2012.
34. Pozar, D. M., *Microwave Engineering*, 256–261, John Wiley & Sons, 2011.